

Orbital Engineering Mediated by Cation Conjugation in Luminescent Uranyl–Organic Hybrid Materials

Adharsh Raghavan,^[a] and Christopher L. Cahill^{*[a]}

[a] Department of Chemistry
The George Washington University
800 22nd St NW, Washington, D.C., USA 20052
E-mail: cahill@gwu.edu

Supporting information for this article is given via a link at the end of the document.

Abstract: A series of compounds of the form $[\text{HAr}]_2[\text{UO}_2\text{X}_4]$ is reported here, wherein Ar is systematically varied between pyridine (**1-X**), quinoline (**2-X**), acridine (**3-X**), 2,5-dimethylpyrazine (**4-X**), quinoxaline (**5-X**), and phenazine (**6-X**), and X = Cl or Br. With greater conjugation in the organic cation, a larger quenching in uranyl luminescence is observed in the solid state. Supporting our luminescence experiments with computation, we map out the potential energy diagrams for the singlet and triplet states of both the $[\text{HAr}]^+$ cations and $[\text{UO}_2\text{Cl}_4]^{2-}$ anion in the crystalline state, and of the assembly. The distinct energy transfer pathways in each compound are discussed.

Introduction

Uranyl tetrahalides are an important class of materials owing to their relevance in nuclear fuel cycle and related settings,^[1] and as illustrative materials for probing electronic structure and bonding of actinyl compounds.^[2,3] The uranyl ion, $[\text{UO}_2]^{2+}$, either in solution or the solid-state, generally emits green light centered at around 520–530 nm, when excited at its characteristic ligand-to-metal charge transfer (LMCT) band at ca. 420 nm.^[3,4] This emission is affected by both primary and secondary coordination sphere influences, and can thus function as a probe of their type and strength, and inform (for example) environmental monitoring and / or forensics applications.^[1,5–9] Luminescence spectroscopy is therefore an appropriate characterization method, given its detection limit in the μM range and applicability to both solution and solid-state samples.^[8] There have been numerous studies delineating the relationship between uranyl emission and the identity and number of equatorial ligands,^[10–15] as well as the presence of metal or organic species and / or other quenchers.^[16–19] Moreover, emission photophysics of photoexcited $(\text{UO}_2^{2+})^*$ can be influenced by participation in chemical reactions.^[4,20] As far as $[\text{UO}_2\text{X}_4]^{2-}$ (X = Cl, Br) species are concerned however, and despite their rich catalogue of compounds, the effects of their interactions with charge-balancing cations on emission spectra have gained interest only recently.^[21–23]

The electronic spectra of uranyl tetrahalides are similar to those of the nominally ‘free’ uranyl ion $[\text{UO}_2]^{2+}$ ($[\text{UO}_2(\text{OH}_2)_5]^{2+}$ in aqueous solution). A classic example is $\text{Cs}_2\text{UO}_2\text{Cl}_4$,^[24] whose absorption features two LMCT bands ($\text{O}_{yl} \rightarrow \text{U}$ and higher energy $\text{Cl} \rightarrow \text{U}$), and emission features the aforementioned green emission characteristic of $[\text{UO}_2]^{2+}$. With the aid of high-resolution

electronic absorption spectra of $\text{Cs}_2\text{UO}_2\text{Cl}_4$,^[24] relativistic density functional theory (DFT),^[25,26] and multiconfigurational perturbation theory (CASSCF/CASPT2) calculations,^[27] the ground and excited state electronic structures of $[\text{UO}_2]^{2+}$ and $[\text{UO}_2\text{Cl}_4]^{2-}$ are now relatively well-understood (Fig. 1).^[3] Generally speaking, the $\text{O}=\text{U}=\text{O}$ bonding situation in $[\text{UO}_2\text{X}_4]^{2-}$ is similar to that in $[\text{UO}_2]^{2+}$, and U–X bonds are predominantly ionic,^[27,28] with a small covalent contribution.^[29,30] In the presence of cations however, the electronic structure of the $[\text{UO}_2\text{X}_4]^{2-}$ moiety is subject to perturbation. Recent work has highlighted the nature and significance of the interactions between equatorial halides and counter-cations in the crystal lattice (e.g. $\text{Cs} \cdots \text{X}$ in $\text{Cs}_2\text{UO}_2\text{X}_4$).^[29–31] Establishing structure-property relationships in materials comprising $[\text{UO}_2\text{X}_4]^{2-}$ charge-balanced by various cations is therefore a step towards further exploring these interactions.

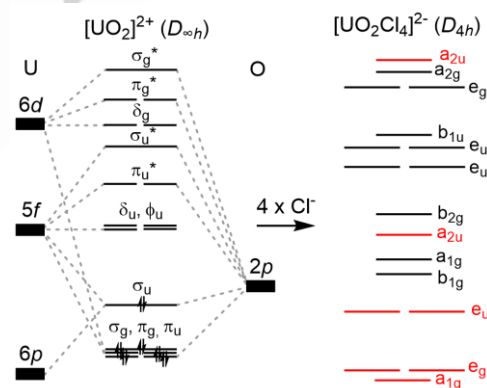


Figure 1. Partial molecular orbital (MO) diagrams for $[\text{UO}_2]^{2+}$ (occupied and vacant orbitals) and $[\text{UO}_2\text{Cl}_4]^{2-}$ (occupied orbitals only, up to HOMO), generated from values in refs [3] and [25]. $[\text{UO}_2\text{Cl}_4]^{2-}$ MOs that have large contributions to U–O bonds are colored red.

We have long been interested in the solid-state assembly of monomeric $[\text{UO}_2\text{X}_4]^{2-}$ units in the presence of organic cations capable of participating in non-covalent interactions (NCIs) such as hydrogen-bonding, halogen-bonding, π - π stacking, $\text{O}_{yl} \cdots \pi$, $\text{X}_{[\text{UO}_2\text{X}_4]^{2-}} \cdots \pi$ and $\text{X}_{\text{cation}} \cdots \text{O}_{yl}$ interactions.^[21,32,33] As our group^[21] and others^[34–42] have shown, the nature and strength of NCIs between $[\text{UO}_2\text{X}_4]^{2-}$ and the counter-cation are indeed reflected in the photophysical properties, and by extension, electronic structure of the materials. In other words, the secondary coordination sphere influences the deactivation pathways of the excited $([\text{UO}_2\text{X}_4]^{2-})^*$ ion. Crystal packing in $[\text{UO}_2\text{X}_4]^{2-}$ -organic hybrid materials provides a rigid framework free from many

deactivation pathways endemic to the solution phase. Energy transfer (EnT) and electron transfer (ET) processes may therefore be expected to play a larger role in solid-state uranyl emission photophysics than in solution.^[4,9] In the present work, we take a systematic approach to tuning EnT and / or ET pathways as a step towards the larger goal of studying *electronic structure-property relationships* in crystalline assemblies containing $[\text{UO}_2\text{X}_4]^{2-}$ species. We have previously explored the use of protonated N-heterocycles ($[\text{HAr}]^+$) with various functional groups in directing supramolecular assembly of uranyl tetrahalide phases. Herein, we turn our attention to extending π -conjugation in $[\text{HAr}]^+$ cations as a strategy to tune the photophysical properties of hybrid materials of the composition $[\text{HAr}]_2[\text{UO}_2\text{X}_4]$ ($\text{X} = \text{Cl}, \text{Br}$). We chose a series of cations ranging from pyridinium to phenazinium (Fig. 2) owing to their ready protonation and tunability of the energy gap between the highest occupied and lowest unoccupied molecular orbitals ($\Delta E_{\text{HOMO-LUMO}}$).

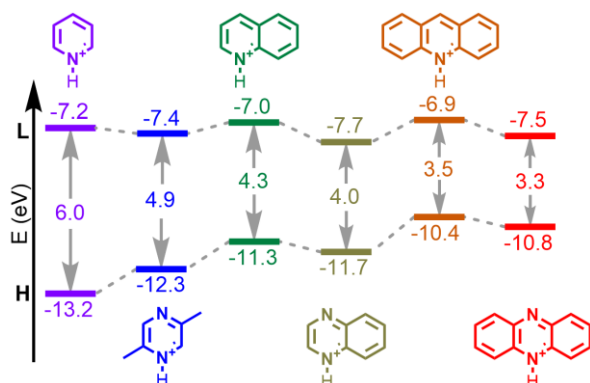


Figure 2. Frontier MOs (H = HOMO and L = LUMO) of the cations employed in this work, calculated at the B3LYP-GD3(BJ)/def2tzvp level (gas phase).

Results and Discussion

Synthesis

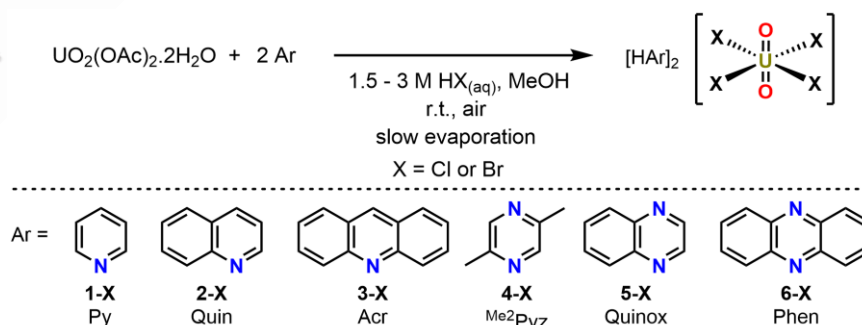
Compounds **1-Cl–6-Cl** and **1-Br–6-Br** (Table 1) were synthesized according to Scheme 1, wherein at high $[\text{X}^-]$ and $[\text{H}^+]$, uranyl halide speciation is restricted to mononuclear species that crystallize as $[\text{UO}_2\text{X}_4]^{2-}$ (Cl, Br) dianions. Eight of the twelve compounds (**2-X**, **3-X**, **5-X**, and **6-X**) discussed here are

previously unreported, and as such were characterized by single-crystal X-ray diffraction analysis. Compounds **1-X** and **4-X** have been reported previously in the Cambridge Structure Database, CSD^[43] (CCDC deposition numbers [1409802](#),^[21] [1409808](#),^[21] 2303972 and 2303973). Crystallographic details of all new compounds are given in the Supporting Information.

Crystal Structures

Compounds **1-X–6-X** ($\text{X} = \text{Cl}, \text{Br}$) all contain the approximately D_{4h} -symmetric $[\text{UO}_2\text{X}_4]^{2-}$ square bipyramid charge-balanced by two $[\text{HAr}]^+$ N-heterocycle monocations. Each compound has one crystallographically unique $[\text{UO}_2\text{X}_4]^{2-}$ moiety (except for **1-Cl** and **2-Cl**, which contain two). The average U=O and U–X distances in the series are 1.769[4] Å and 2.670[3] Å respectively for the chlorides, and 1.773[4] Å and 2.8197[4] for the bromides (Table 1). These values are unremarkable and well within the reported range for each metric in the 85 uranyl tetrachloride and 32 uranyl tetrabromide-containing structures in the CSD ($[\text{UO}_2\text{Cl}_4]^{2-}$: $d_{\text{U=O,CSD}} = 1.764[19]$ Å and $d_{\text{U-Cl,CSD}} = 2.671[21]$ Å; $[\text{UO}_2\text{Br}_4]^{2-}$: $d_{\text{U=O,CSD}} = 1.761[27]$ Å and $d_{\text{U-Br,CSD}} = 2.281[15]$ Å). In all compounds, the O=U=O angle is 180°, and O=U–X and *cis* X–U–X angles are ca. 90°. Complete crystallographic data for **2-X**, **3-X**, **5-X**, and **6-X** are provided in the Supporting Information.

Turning to the packing of $[\text{UO}_2\text{X}_4]^{2-}$ with the various cations, hydrogen bonding to the uranyl tetrahalide unit occurs in all compounds with the exceptions of **2-Br** and **4-X**. In each case, one of the two crystallographically unique halide pairs *trans* to each other is engaged in N–H \cdots X H-bonding (Figure 3). As a result, there is a slight distortion from the ideal D_{4h} $[\text{UO}_2\text{X}_4]^{2-}$ square pyramidal geometry to D_{2h} . Other NCIs involving the $[\text{UO}_2\text{X}_4]^{2-}$ dianion include N–H \cdots Oyl, Br \cdots O_{water}, Br \cdots Br, Oyl \cdots π and X \cdots π interactions. Despite being weak interactions on the order of a few kcal/mol,^[44] all of these NCIs play a role in assembling the centroids of $[\text{HAr}]^+$ cations within 10 Å of the U atoms of the neighboring $[\text{UO}_2\text{X}_4]^{2-}$ square bipyramids (Table S9 and Figs. S13–S24). We highlight these relevant, although subtle crystallographic features here as support for discussions of energy transfer (below).



Scheme 1. Synthesis of compounds **1-X** – **6-X**.

Table 1. Selected structural parameters of 1-X—6-X

Compound	U–O (Å)	U–X (Å)	Primary NCIs
*1-Cl, [C ₉ H ₆ N] ₂ [UO ₂ Cl ₄] ^[21]	1.772[3] [#]	2.6685[8] [#]	N-H...Cl, π-π
*2-Cl, [C ₉ H ₆ N] ₂ [UO ₂ Cl ₄]	U1–O1: 1.763(2) U2–O2: 1.768(3)	U1–Cl1: 2.6530(9) U1–Cl2: 2.6746(10) U2–Cl3: 2.6601(10) U2–Cl4: 2.6865(9)	N-H...Cl2, N-H...Cl4, π-π
3-Cl, [C ₁₃ H ₁₀ N] ₂ [UO ₂ Cl ₄]	1.766(7)	U1–Cl1: 2.694(2) U1–Cl2: 2.658(2)	N-H...Cl1
4-Cl, [C ₆ H ₉ N ₂] ₂ [UO ₂ Cl ₄]	1.766(2)	U1–Cl1: 2.6629(9) U1–Cl2: 2.6846(8)	Cl1...π, O _{y1} ...π, N-H...N
5-Cl, [C ₈ H ₇ N ₂] ₂ [UO ₂ Cl ₄]	1.7802(19)	U1–Cl1: 2.6380(7) U1–Cl2: 2.6587(6)	N-H...O _{y1} , N-H...Cl2, π-π
6-Cl, [C ₁₂ H ₉ N] ₂ [UO ₂ Cl ₄]	1.770(3)	U1–Cl1: 2.6578(9) U1–Cl2: 2.6957(9)	N-H...Cl2, π-π, Cl2...π
1-Br, [C ₉ H ₆ N] ₂ [UO ₂ Br ₄] ^[21]	1.7689(16)	U1–Br1: 2.8372(2) U1–Br2: 2.8186(2)	N-H...Br1, O _{y1} ...π
2-Br, [C ₉ H ₆ N] ₂ [UO ₂ Br ₄]·2H ₂ O	1.774(4)	U1–Br1: 2.8164(7) U1–Br2: 2.8221(7)	HO _w -H...Br
3-Br, [C ₁₃ H ₁₀ N] ₂ [UO ₂ Br ₄]	1.772(4)	U1–Br1: 2.8102(5) U1–Br2: 2.8258(6)	N-H...Br2, Br2...Br2'
4-Br, [C ₆ H ₉ N ₂] ₂ [UO ₂ Br ₄]	1.766(3)	U1–Br1: 2.8101(4) U1–Br2: 2.8293(3)	Br1...π, N-H...N
5-Br, [C ₈ H ₇ N ₂] ₂ [UO ₂ Br ₄]	1.775(4)	U1–Br1: 2.8248(6) U1–Br2: 2.7918(6)	N-H...Br1, π-π, O _{y1} ...π
6-Br, [C ₁₂ H ₉ N] ₂ [UO ₂ Br ₄]	1.762(4)	U1–Br1: 2.8073(6) U1–Br2: 2.8385(6)	N-H...Br2, π-π, Br2...π

*1-Cl and 2-Cl have two crystallographically unique [UO₂Cl₄]²⁻ moieties. # Averaged values

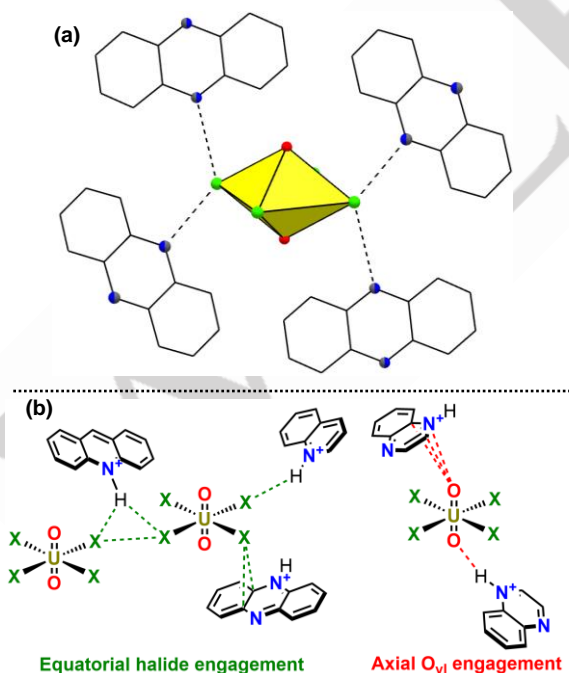


Figure 3. (a) Polyhedral representation of the [UO₂Cl₄]²⁻ square bipyramid in 3-Cl along with N(-H)...Cl Hydrogen-bonding interactions stemming from neighboring [HAcrl]⁺ moieties. [HAcrl]⁺ ions are disordered about an inversion center; N1 and C1A atoms (blue and grey hemispheres respectively) occupy the same sites with 50 % occupancy each. O and Cl atoms are represented as

red and green spheres, respectively. (b) Skeletal representation of the various NCIs present in compounds 1-X—6-X.

Electronic Structures

Compounds 1-Cl to 3-Cl, in which the cations vary from pyridinium to quinolinium to acridinium, serve as representative examples to illustrate the effect of increased conjugation in [HAr]⁺ on the properties of these materials. We will therefore discuss these materials in depth, whereas crystallographic, spectroscopic, and computational details regarding all other compounds can be found in the Supporting Information.

Diffuse Reflectance Spectroscopy

Solid-state diffuse reflectance spectra (Fig. 4) show that compounds 1-Cl—3-Cl have intense absorptions in the UV (200—380 nm) that can be attributed primarily to high-energy n/π→π* transitions in [HAr]⁺, and Cl→U LMCT transitions in [UO₂Cl₄]²⁻. The uranyl-based O→U LMCT absorption bands with vibrational structuring are clearly visible for 1-Cl and 2-Cl in the 385—500 nm region. For 3-Cl however, on account of a much smaller ΔE_{HOMO-LUMO} in [HAcrl]⁺, the uranyl-based bands overlap strongly with acridinium-based lower-energy π→π* transitions.

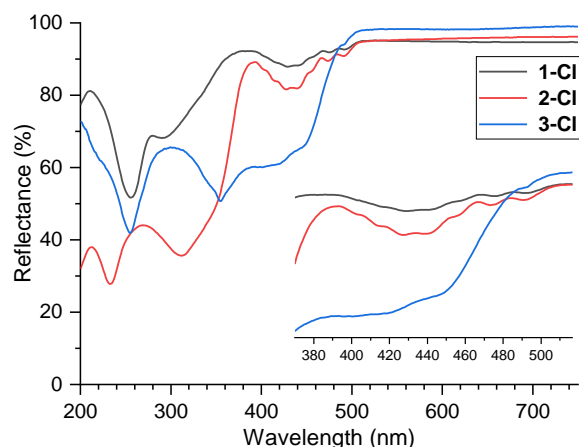


Figure 4. Diffuse reflectance spectra (ca. 5 wt% in BaSO₄) of **1-CI**–**3-CI**. Inset shows O_{yl}→U LMCT region.

Luminescence Spectroscopy

Luminescence spectra for compounds **1-CI**–**3-CI** collected at 78 K and 298 K are shown in Figures 5 and S25 respectively. **1-CI** has been characterized previously by our group; emission and excitation profiles, and relative peak intensities, collected on freshly prepared samples of **1-CI** agree with our previous work.^[21] **1-CI** and **2-CI** exhibit typical uranyl luminescence (top and middle panels of Fig. 5), with **2-CI** having a smaller photoluminescence quantum yield compared to **1-CI** (Table S10). Low temperature spectra helped identify two major coupling modes associated with

[UO₂]²⁺ (Tables S11 and S13). The Raman-active symmetric O=U=O stretching mode (ν_1) couples to the triplet excited state in a similar fashion in both compounds (831 ± 16 cm⁻¹ in **1-CI**, 830 ± 15 cm⁻¹ in **2-CI**). A second, much lower energy mode was also identified (258 ± 17 cm⁻¹ in **1-CI**, 246 ± 14 cm⁻¹ in **2-CI**) and assigned as the O=U=O bending mode (ν_2).^[8,23] Further details on the fine structure of uranyl luminescence within each vibronic progression can be found in the Supporting Information (Tables S11–S17).

The excitation spectra in Figure 5 have two important features. The broad peak centered at ca. 340 nm for **1-CI** and 365 nm for **2-CI** consists of an LMCT excitation from predominantly equatorial Cl *p* orbitals to U 5*f* orbitals. Considering that the U–Cl bond lengths in both molecules are similar, this difference of ca. 25 nm may be attributed to overlap with [HQuin]⁺ absorption and minor differences in the NCIs between [UO₂Cl₄]²⁻ and [HAr]⁺. The more structured set of peaks between 370 and 500 nm in **1-CI** and between 380 and 500 nm in **2-CI** correspond to axial O_{yl}-based LMCT. Compared to the equatorial Cl→U LMCT, the uranyl-localized LMCT is invariant in the two complexes, a sign of negligible perturbation of the linear UO₂²⁺ moiety in the crystalline state, as corroborated by a lack of meaningful short-contacts to O_{yl} from neighboring pyridinium or quinolinium cations in **1-CI** and **2-CI**. Additionally, **2-CI** also exhibits a very weak emission in the 380–420 nm range, attributable to [HQuin]⁺ fluorescence (Fig. S25).

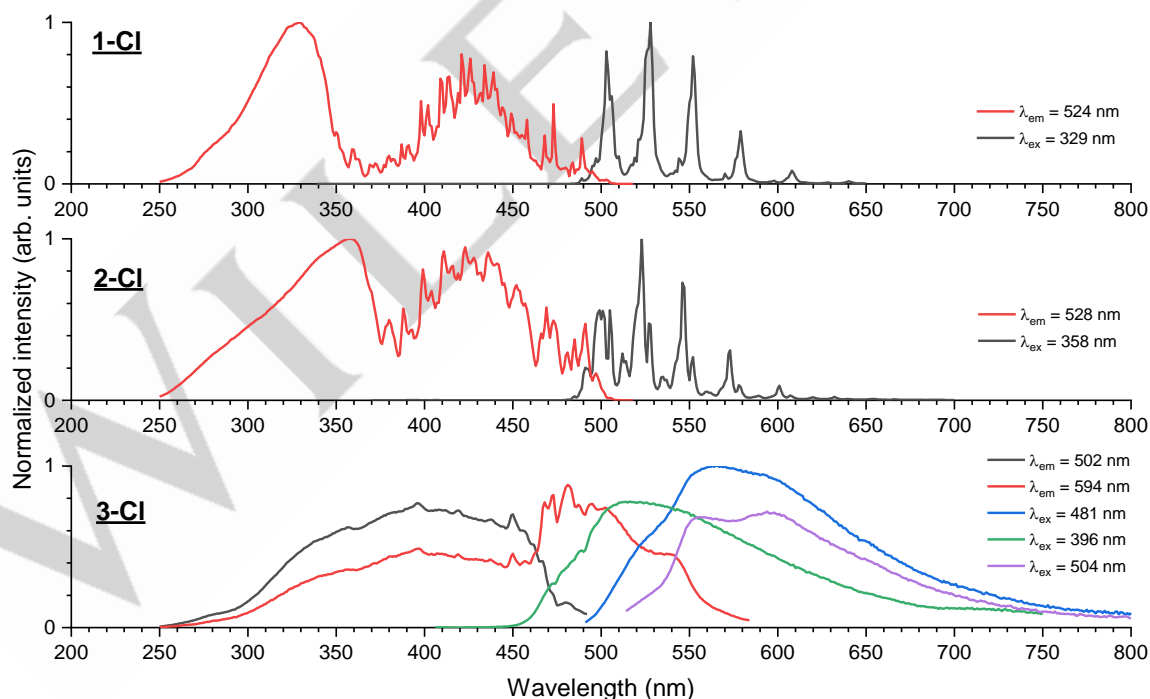


Figure 5. Low temperature (78 K) luminescence spectra of **1-CI** (top), **2-CI** (middle) and **3-CI** (bottom). Emission and excitation spectra are labelled with their corresponding λ_{ex} and λ_{em} , respectively.

Luminescence of 3-CI

While increasing π -conjugation from pyridinium to quinolinium did not significantly affect the [UO₂Cl₄]²⁻ luminescence, the story with

acridinium is quite different. Neither the emission nor excitation spectrum of **3-CI** has any identifiable [UO₂Cl₄]²⁻-like features (bottom panel of Fig. 5). Instead, they more closely resemble that of acridinium chloride ([HAc]Cl, Fig. S26). It is useful to note here

that at both 298 K and 78 K, the excitation and emission spectra of [HAc]Cl are qualitatively similar; the tail of the excitation spectrum is limited to 240–500 nm, and the emission spectrum to 380–650 nm (Fig. S26). Compound **3-Cl** exhibits several features that are neither attributable to $[\text{UO}_2\text{Cl}_4]^{2-}$ nor solely to [HAc]Cl. For instance, while there is a very broad, mostly featureless emission with $\lambda_{\text{max,em}}$ of ca. 502 nm (green trace, Fig. 5) when excited anywhere between 300 nm and 450 nm, there are no low-intensity peaks that precede the major peak at 502 nm or the shoulder peak(s) at 470 nm. This is in stark contrast to [HAc]Cl which shows a few emission peaks in the 350–440 nm range, corresponding to emission from higher excited states.^[45] Secondly, a new broad emission feature from 500–800 nm emerges when **3-Cl** is excited at $\lambda > 450$ nm (blue and purple traces, bottom panel of Fig. 5). A corresponding ($\lambda_{\text{em}} = 650$ nm) broad excitation feature can be seen between 470 nm and 590 nm (red trace). Note that both features have no equivalents in the steady-state spectra of [HAc]Cl (Fig. S26). We hypothesize, based on previous work on Acr and [HAc]⁺, that these peaks correspond to phosphorescence from the acridinium cations in **3-Cl**.^[45–50] This comports well with the literature; upon excitation, [HAc]⁺ shows a high fluorescence quantum yield and negligible triplet state population.^[48] The purple trace in Figure 5 suggests that the acridinium triplet state (T_1) in **3-Cl** lies ca. 2 eV above the ground state (S_0).

Lifetime measurements on all three compounds **1-Cl**–**3-Cl** at $\lambda_{\text{ex}} = 356$ nm provide some preliminary evidence for emission from triplet states (either $[\text{UO}_2\text{Cl}_4]^{2-}$ or [HAc]⁺). **1-Cl** and **2-Cl** exhibit typical uranyl luminescence as mentioned previously. Emission decay was found to be independent of the wavelength chosen for monitoring: for $500 \text{ nm} < \lambda_{\text{em}} < 600$ nm, the decays for both compounds obeyed first-order kinetics. Mono-exponential fits gave lifetimes (τ) of $28.8 \pm 0.1 \mu\text{s}$ for **1-Cl** and $29.2 \pm 0.2 \mu\text{s}$ for **2-Cl** (pg S45); both values are in excellent agreement with the value of $34.8 \mu\text{s}$ measured for $[\text{UO}_2\text{Cl}_4]^{2-}$ by Natrajan and co-workers.^[51] The case for **3-Cl** is however, quite different. We confirmed that there are no $[\text{UO}_2\text{Cl}_4]^{2-}$ emission characteristics to the broad emission profile of **3-Cl** by measuring lifetimes at wavelengths between 450–600 nm (Fig. 6, Table 2 and pg S38–S44). Instead, the decay is wavelength-dependent, not unlike HAc⁺,^[45,50,52] requiring bi-exponential fits. Two emission lifetimes at 500 and 600 nm (τ_1 and τ_2) were extracted from solid-state samples of **3-Cl** and [HAc]Cl. When λ_{em} was swept from 450 nm to 600 nm, the rate of decay of the excited state(s) steadily increased, with the longer-lived component (τ_2 in Table 2) gaining weight in the bi-exponential function. Notably at 600 nm, τ_2 of **3-Cl** is at least an order of magnitude larger than any of the τ_1 s of [HAc]Cl.

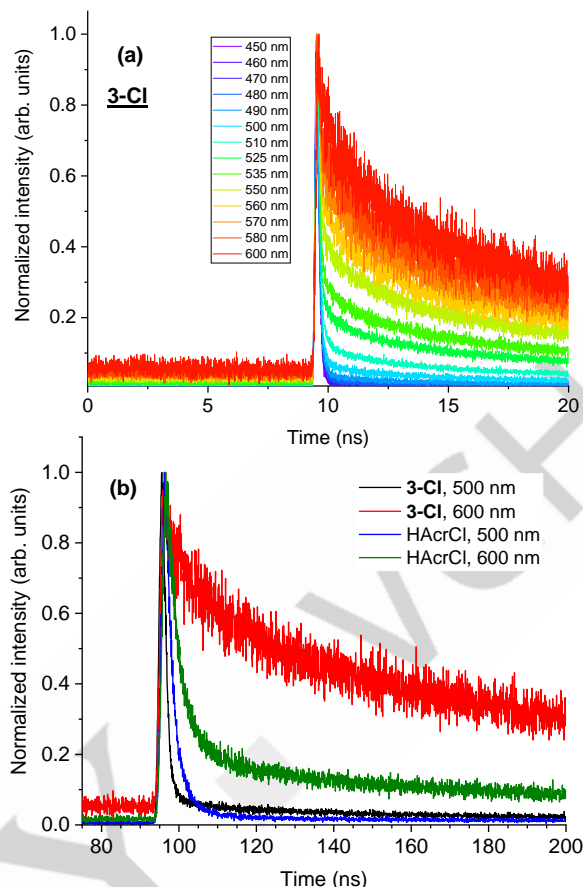


Figure 6. Emission decay data for (a) **3-Cl** measured at different emission wavelengths and (b) **3-Cl** and [HAc]Cl measured at 500 and 600 nm. $\lambda_{\text{ex}} = 356$ nm, $T = 298$ K.

Table 2. Lifetimes and % contributions of each decay component associated with decay of emission at 500 nm and 600 nm for [HAc]Cl and **3-Cl**; $T = 298$ K, $\lambda_{\text{ex}} = 356$ nm.

Compound	λ_{em} (nm)	τ_1 (ns)	τ_2 (ns)
[HAc]Cl	500	2.2 ± 0.2 (71%)	22.8 ± 1.4 (29%)
	600	3.4 ± 0.7 (25%)	48.3 ± 2.0 (75%)
3-Cl	500	1.0 ± 0.2 (25%)	36.8 ± 1.1 (75%)
	600	64.5 ± 1.6 (18%)	405.8 ± 4.0 (82%)

*Additional data on **1-Cl**–**3-Cl**, along with fitting parameters, reduced χ^2 values, and residuals can be found in the Supporting Information.

Overall, two things become apparent: (i) When **3-Cl** is excited at 356 nm, a prime wavelength for both uranyl tetrachloride and acridinium absorption, there is no uranyl-based emission whatsoever, and (ii) while some of the emission is short-lived acridinium-based fluorescence, the compound likely also phosphoresces both at 298 K and 78 K, when excited at longer wavelengths ($\lambda_{\text{ex}} > 450$ nm). The near-complete overlap of $[\text{UO}_2\text{Cl}_4]^{2-}$ and [HAc]⁺ absorptions in the 300–500 nm range, and large overlap of $[\text{UO}_2\text{Cl}_4]^{2-}$ emission and [HAc]⁺-based excitation peaks in the 500–550 nm range (that correspond to longer-lived phosphorescence at $\lambda > 550$ nm; purple and blue traces in Fig. 5) make it difficult to pin-point the exact mechanism by which [HAc]⁺ excited states (both singlet and triplet) are populated. The clear indication from experiments, however, is that

the energy transfer between $[\text{UO}_2\text{Cl}_4]^{2-}$ and $[\text{HAc}r]^+$ is feasible and quite efficient. In other words, the emissive states of **3-CI**, either a singlet or triplet state of $[\text{HAc}r]^+$, are both energetically accessible from $(\text{UO}_2^{2+})^*$ (see DFT discussion below). Indeed, these observations agree well with the luminescence behavior of *all* compounds (**1-CI**–**6-CI**) presented here. We note cations with HOMO–LUMO gap ≤ 3.5 eV (from gas-phase DFT calculations) appear to efficiently quench $[\text{UO}_2\text{Cl}_4]^{2-}$ luminescence. The effect of increasing π conjugation in $[\text{HAr}]^+$ on uranyl emission among the two homologous series, **1-CI**–**3-CI** and **4-CI**–**6-CI**, is thus readily apparent.

Table 3. Luminescence characteristics of **1-CI**–**6-CI** at 298 K and 78 K

Compound	Cation	Luminescence		$\Delta E_{\text{HOMO-LUMO, [HAr]}^+}$ (eV)*
		298 K	78 K	
1-CI	$[\text{HPy}]^+$	$[\text{UO}_2]^{2+}$	$[\text{UO}_2]^{2+}$	6.0
2-CI	$[\text{HQuin}]^+$	$[\text{UO}_2]^{2+}$	$[\text{UO}_2]^{2+}$	4.3
3-CI	$[\text{HAc}r]^+$	$[\text{HAc}r]^+$	$[\text{HAc}r]^+$	3.5
4-CI	$[\text{H}^{2,5\text{Me}_2\text{Pyz}}]^+$	$[\text{UO}_2]^{2+}$	$[\text{UO}_2]^{2+}$	4.9
5-CI	$[\text{HQuinox}]^+$	$[\text{HAr}]^+$	$[\text{UO}_2]^{2+}$ (minor) and $[\text{HAr}]^+$	4.0
6-CI	$[\text{HPhen}]^+$	$[\text{HAr}]^+$	$[\text{HAr}]^+$	3.3

*Values obtained from gas-phase DFT calculations (cf. Fig. 2).

Density Functional Theory (DFT) Calculations

Ground-state and time-dependent DFT calculations provide insight into the spectroscopic and electronic structure trends in compounds **1-CI** to **3-CI**. A simplified view of the ground-state crystal orbitals obtained by imposing periodic boundary conditions (PBC) is shown in Figure 7 in the form of density of states (DOS), delineated into uranyl tetrachloride and organic cation-based orbitals. DFT tends to overestimate the bandgap of these materials, especially in the absence of a Hubbard U correction or plane-wave basis sets, nevertheless even this crude periodic DFT calculation shows qualitative agreement with the results of the more accurate plane-wave DFT calculations on uranyl tetrachloride systems from the Forbes and Mason groups.^[37,38] Considering that uranyl emission arises from an $S = 1$ state, we also calculated the singlet and triplet energy levels of isolated, geometry optimized $[\text{UO}_2\text{Cl}_4]^{2-}$ and $[\text{HAr}]^+$ ions in the gas phase ($\{[\text{UO}_2\text{Cl}_4]^{2-}\}_{\text{gas}}$ and $\{[\text{HAr}]^+\}_{\text{gas}}$), and within a field of point charges ($\{[\text{UO}_2\text{Cl}_4]^{2-}\}_{\text{xtal}}$ and $\{[\text{HAr}]^+\}_{\text{xtal}}$). Point charges were derived from natural population analysis (NPA) of an ensemble of either $[\text{UO}_2\text{Cl}_4]^{2-}$ or $[\text{HAr}]^+$, along with their neighbors within a sphere of radius 10 Å. This served as an approximation of the electrostatic field experienced by the moiety of interest. The orbital energies calculated in this manner for $\{[\text{UO}_2\text{Cl}_4]^{2-}\}_{\text{xtal}}$ and $\{[\text{HAr}]^+\}_{\text{xtal}}$ were in excellent agreement with the corresponding values obtained from periodic DFT calculations. In **1-CI**–**3-CI**, the HOMO and LUMO levels of $[\text{HAr}]^+$ are perturbed relative to their respective gas-phase energy levels. $\Delta E_{\text{HOMO-LUMO}}$ of $\{[\text{HPy}]^+\}_{\text{xtal}}$, $\{[\text{HQuin}]^+\}_{\text{xtal}}$, and $\{[\text{HAc}r]^+\}_{\text{xtal}}$ are respectively 5.6, 3.7, and 2.8 eV (cf. 6.0, 4.3, and 3.5 eV; Fig. 2). Full details of the computational methodology can be found in the Supporting Information.

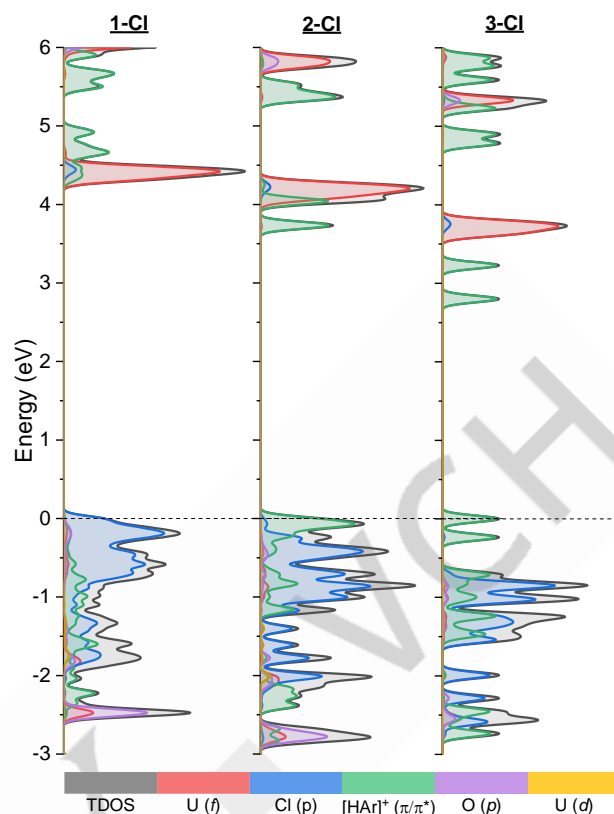


Figure 7. Total (TDOS) and projected density of states for compounds **1-CI** – **3-CI**. **The dotted line at 0 eV corresponds to highest occupied crystal orbitals (HOCO).

Moving from pyridinium to quinolinium to acridinium, the highest occupied and lowest unoccupied crystal orbitals (HOCO and LUCO) switch from exclusively $[\text{UO}_2\text{Cl}_4]^{2-}$ -based in **1-CI** to exclusively $[\text{HAr}]^+$ -based in **2-CI** and **3-CI**. Using a point-charge model as described above, we estimated the singlet–triplet energy gaps (ΔE_{ST}) of $\{[\text{HAr}]^+\}_{\text{xtal}}$ and $\{[\text{UO}_2\text{Cl}_4]^{2-}\}_{\text{xtal}}$ and placed the lowest triplet levels (T_1) of each moiety relative to the energies of the orbitals obtained from periodic DFT calculations (Fig. 8). This energy scheme allows for a direct analysis of $[\text{UO}_2\text{Cl}_4]^{2-}$ and $[\text{HAr}]^+$ frontier orbitals terms of ‘donor’ and ‘acceptor’ moieties, which are relevant for elucidating the mechanism(s) of EnT and / or ET. With increasing conjugation, the T_1 state local to $[\text{HAr}]^+$ ($T_{1,[\text{HAr}]^+}$) is lowered in energy relative to the emissive T_1 state of $[\text{UO}_2\text{Cl}_4]^{2-}$ ($T_{1,\text{Ur}}$), until in **3-CI**, $T_{1,\text{Ur}}$ lies below $T_{1,[\text{HAr}]^+}$. Thus in **1-CI** and **2-CI**, we observe typical uranyl emission out of $T_{1,\text{Ur}}$, while in **3-CI**, this state likely gets depopulated as a result of efficient EnT and / or ET to $T_{1,[\text{HAr}]^+}$ (see discussion below). The latter process is energetically unfavorable in **1-CI** and **2-CI**. Overall, Figure 8 nicely explains why in **1-CI** we see uranyl phosphorescence, in **2-CI** primarily uranyl phosphorescence and negligible $[\text{HQuin}]^+$ fluorescence, and in **3-CI** exclusively $[\text{HAc}r]^+$ fluorescence and phosphorescence. More broadly, our computations support the observation that among the uranyl tetrachloride phases studied, the ones whose $\{[\text{HAr}]^+\}_{\text{xtal}}$ cations have $\Delta E_{\text{HOMO-LUMO}} \leq 2.8$ eV exhibit no uranyl-based emission either at 298 K or 78 K (Table 3).

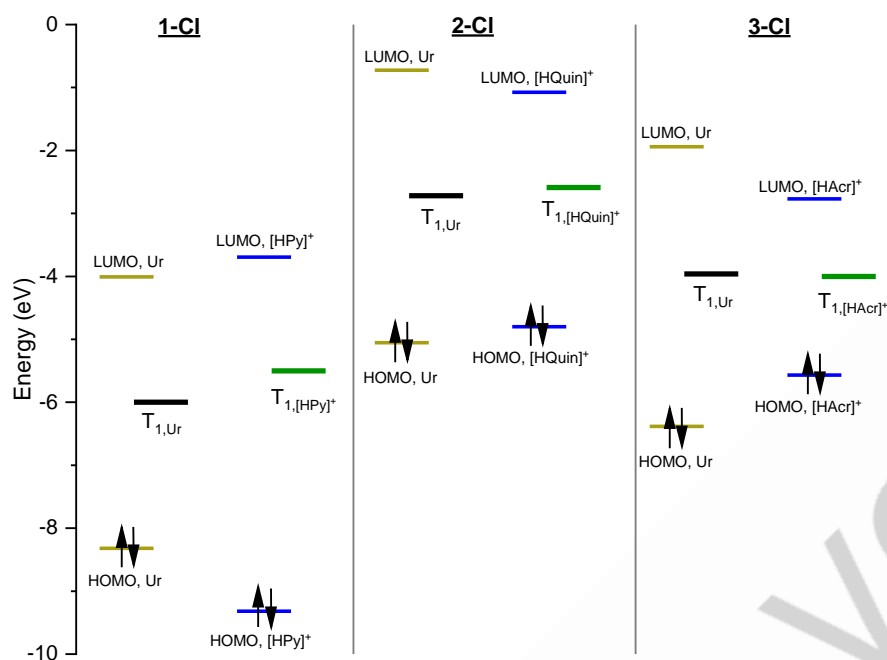


Figure 8. Frontier orbital diagrams of **1-CI–3-CI** of predominantly (> 75%) $[\text{UO}_2\text{Cl}_4]^{2-}$ (dark yellow) or $[\text{HAr}]^+$ (blue) character, based on periodic DFT calculations. The triplet excited state energy levels (T_1) of $[\text{UO}_2\text{Cl}_4]^{2-}$ and $[\text{HAr}]^+$ relative to their respective highest filled orbitals are inserted as thick black and green lines, respectively (see text and Supporting Information for computational details).

Energy Transfer: Discussion

Matsushima and co-workers have studied uranyl luminescence quenching by aromatic hydrocarbons extensively.^[18,19] Being a potent photooxidant, the predominant modes of reactivity of $(\text{UO}_2^{2+})^*$ in the presence of organic molecules are organic radical formation and subsequent degradation through intermolecular ET, and the formation of $[\text{O}=\text{U}^{\text{V}}-\text{O}-\text{H}]^{2+}$ species *via* hydrogen-atom transfer (HAT),^[4,20] Applying these observations to our system (**3-CI**), HAT from or decomposition of $[\text{HAc}r]^+$ do not appear to be present, since there is no change to the luminescence spectra upon prolonged exposure of crystals of **3-CI** (4–5 hours) to either 350–360 nm or ca. 420 nm light under inert conditions (Fig. S33). Moreover, all the spectra reported here are steady-state spectra, suggesting that intermolecular ET processes, if occurring, are likely followed by rapid back-electron transfer and / or non-radiative decay.

A closer look at the low temperature luminescence spectra (bottom panels of Figures 5 and S25) reveals significant overlap between typical uranyl emission peaks (cf. **1-CI** and **2-CI**) and the excitation spectrum of **3-CI**. The overlap is nearly complete with the broad excitation feature between 450–600 nm corresponding to λ_{em} of 650 nm, and partial for the excitation spectrum corresponding to λ_{em} of 504 nm. The emission peak at ca. 600 nm however, appears as a well-resolved peak only when $\lambda_{\text{ex}} > 480$ –500 nm. A considerable overlap of the two emissions resulting from λ_{ex} of 396 nm and 500 nm make it difficult to deconvolute the emission spectra obtained when $340 < \lambda_{\text{ex}} < 500$ nm. Nevertheless, considering that the centroids of neighboring acridinium cations are all placed within 10 Å of the $[\text{UO}_2\text{Cl}_4]^{2-}$ unit, Förster Resonance Energy Transfer (FRET) is one plausible mechanism of EnT.^[53] Since FRET depends on dipole-dipole coupling and does not have spin restrictions, the depopulation of $T_{1,\text{Ur}}$ likely results in the eventual population of $S_{1,\text{HAc}r+}$.

Yet another plausible mechanism for uranyl emission quenching in **3-CI** is Dexter energy transfer (DET).^[53,54] The distance requirement for DET is stringent, with the donor and acceptor molecules typically being separated by no more than 10 Å, and this is met by **3-CI** (Fig. S19 and Table S17). The excitation to the lowest excited state of the $[\text{UO}_2\text{Cl}_4]^{2-}$ anion from its ground state orbitals may be thought of as proceeding through a net $\text{Cl} \rightarrow \text{U}$ charge transfer, creating a partial hole on the Cl *p* orbitals, and populating a higher energy orbital primarily composed of U (*f*) character. The appropriately spaced HOMO—LUMO energy gaps of $[\text{UO}_2\text{Cl}_4]^{2-}$ and $[\text{HAr}]^+$ as seen from Figure 8, and the mixing of filled $[\text{HAc}r]^+$ and $[\text{UO}_2\text{Cl}_4]^{2-}$ orbitals (Fig. S34) make DET a viable mechanism for EnT. DET also provides an alternate explanation for the direct population of $T_{1,[\text{HAc}r]^+}$ from $T_{1,\text{Ur}}$ in **3-CI** (thermodynamically unfavorable in **1-CI** and **2-CI**; Fig. 8). It is worth noting here that triplet-triplet EnT from inorganic anions to organic cations has been observed to proceed through DET in hybrid materials comprising lead bromide and naphthalene-based ammonium layers,^[55,56] lending credence to the possibility of a DET mechanism in a hybrid material with *no significant* covalent bonding between donor and acceptor. Overall, the mechanism of EnT in the solid-state is not clear at this stage. Future experiments on systems similar to **3-CI** will explore the relationship between the separation between $[\text{HAr}]^+$ and $[\text{UO}_2\text{X}_4]^{2-}$, spectral overlap between donor and acceptor, wavefunction overlap, and rate and efficiency of energy transfer.

Whereas we have thus far focused exclusively on $[\text{UO}_2\text{Cl}_4]^{2-}$, we note here that the $[\text{UO}_2\text{Br}_4]^{2-}$ phases (**1-Br–6-Br**) behave rather similarly. The trends in luminescence are identical, and similar inferences regarding EnT mechanisms may be made. The Supporting Information contains all relevant information (crystal structures, spectroscopy, and computation) for this analogous family of compounds.

Conclusion

We have reported here the syntheses and characterization of two series of uranyl tetrachlorides and tetrabromides of the form $[\text{HAr}]_2[\text{UO}_2\text{X}_4]$, wherein the cations $[\text{HAr}]^+$ were systematically varied based on their extent of π conjugation. It became clear from both experiment and computation, that cations with $\Delta E_{\text{HOMO-LUMO}} \leq 3.5$ eV in the gas-phase, and more importantly with triplet excited states lying close to or below the T_1 of $[\text{UO}_2\text{Cl}_4]^{2-}$ efficiently quench uranyl-based luminescence. While $[\text{UO}_2]^{2+}$ emission quenching has long been known and studied, the simple system $[\text{HAr}]_2[\text{UO}_2\text{X}_4]$ offers a platform with which to study this phenomenon in the solid state, with particular focus on secondary coordination sphere interactions with cations with tunable frontier orbital energies. Our future efforts in this area will focus on elucidating the exact mechanism(s) of energy transfer and / or electron transfer between uranyl-bearing systems and appropriately chosen organic moieties. This in turn is expected to yield a deeper understanding of the electronic structure and tunability of actinide-bearing hybrid materials.

Supporting Information

Supplementary data (experimental details, powder XRD patterns, single-crystal XRD data, luminescence spectra, emission decay analyses, and computational details) associated with this article can be found online at xxx<insert doi>xxx. Crystallographic information on compounds^[67] can be obtained free of charge by e-mailing data_request@ccdc.cam.ac.uk or by contacting The Cambridge Crystallographic Data Centre, 12 Union Road, Cambridge, CB2 1EZ UK; Fax +44(0)1223-336033; http://www.ccdc.cam.ac.uk/data_request/cif.

Acknowledgements

This work was supported by the U.S. Department of Energy Office of Science, Office of Basic Energy Sciences, Division of Chemical Sciences, Geosciences, and Biosciences, Heavy Element Chemistry program under grant DE-FG02-05ER15736. This work was completed in part with resources provided by the High Performance Computing Cluster at The George Washington University, Research Technology Services.

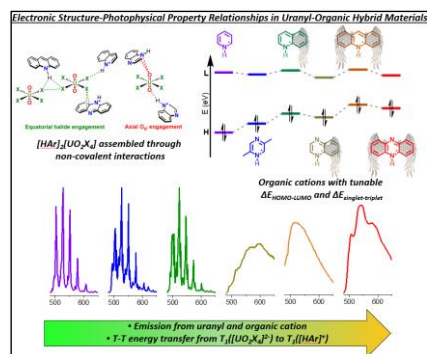
Keywords: uranyl • actinide • photoluminescence • photophysics • energy transfer

- [1] J. J. Katz, G. T. Seaborg, L. R. Morss, *The Chemistry of the Actinide Elements: Volume 2*, Springer, **1987**.
- [2] R. G. Surbella, L. C. Ducati, K. L. Pellegrini, B. K. McNamara, J. Autschbach, J. M. Schwantes, C. L. Cahill, *J. Am. Chem. Soc.* **2017**, *139*, 10843–10855.
- [3] R. G. Denning, *J. Phys. Chem. A* **2007**, *111*, 4125–4143.
- [4] H. D. Burrows, T. J. Kemp, *Chem. Soc. Rev.* **1974**, *3*, 139.
- [5] A. H. Saller, A. M. Stueber, *AAPG Bull.* **2018**, *102*, 401–428.
- [6] S. J. Lambert, *Appl. Geochem.* **1992**, *7*, 513–531.
- [7] J. F. Lucchini, M. Borkowski, M. K. Richmann, D. T. Reed, *Radiochim. Acta* **2013**, *101*, 391–398.
- [8] G. Lu, A. J. Haes, T. Z. Forbes, *Coord. Chem. Rev.* **2018**, *374*, 314–344.
- [9] E. Rabinowitch, R. L. Belford, *Spectroscopy and Photochemistry of Uranyl Compounds: International Series of Monographs on Nuclear Energy*, Elsevier, **2013**.
- [10] P. Thuéry, E. Rivière, J. Harrowfield, *Inorg. Chem.* **2015**, *54*, 2838–2850.
- [11] P. Thuéry, J. Harrowfield, *Cryst. Growth Des.* **2014**, *14*, 1314–1323.
- [12] P. Thuéry, J. Harrowfield, *CrystEngComm* **2015**, *17*, 4006–4018.
- [13] Y. Zhang, I. Karatchevseva, J. R. Price, I. Aharonovich, F. Kadi, G. R. Lumpkin, F. Li, *RSC Adv.* **2015**, *5*, 33249–33253.
- [14] M. P. Redmond, S. M. Cornet, S. D. Woodall, D. Whittaker, D. Collison, M. Helliwell, L. S. Natrajan, *Dalton Trans.* **2011**, *40*, 3914.
- [15] C. Görller-Walrand, S. De Jaegere, *Spectrochim. Acta Part Mol. Spectrosc.* **1972**, *28*, 257–268.
- [16] H. D. Burrows, S. J. Formosinho, *J. Chem. Educ.* **1978**, *55*, 125.
- [17] H. D. Burrows, S. J. Formosinho, M. D. G. Miguel, F. P. Coelho, *J. Chem. Soc. Faraday Trans. 1 Phys. Chem. Condens. Phases* **1976**, *72*, 163.
- [18] R. Matsushima, *J. Am. Chem. Soc.* **1972**, *94*, 6010–6016.
- [19] R. Matsushima, S. Sakuraba, *J. Am. Chem. Soc.* **1971**, *93*, 7143–7145.
- [20] B. E. Cowie, J. M. Purkis, J. Austin, J. B. Love, P. L. Arnold, *Chem. Rev.* **2019**, *119*, 10595–10637.
- [21] R. G. Surbella, M. B. Andrews, C. L. Cahill, *J. Solid State Chem.* **2016**, *236*, 257–271.
- [22] H. Oher, T. Vercouter, F. Réal, C. Shang, P. E. Reiller, V. Vallet, *Inorg. Chem.* **2020**, *59*, 15036–15049.
- [23] H. Oher, F. Réal, T. Vercouter, V. Vallet, *Inorg. Chem.* **2020**, *59*, 5896–5906.
- [24] R. G. Denning, T. R. Snellgrove, D. R. Woodwark, *Mol. Phys.* **1976**, *32*, 419–442.
- [25] R. G. Denning, J. C. Green, T. E. Hutchings, C. Dallera, A. Tagliaferri, K. Giarda, N. B. Brookes, L. Braicovich, *J. Chem. Phys.* **2002**, *117*, 8008–8020.
- [26] K. Pierloot, E. Van Besien, E. Van Lenthe, E. J. Baerends, *J. Chem. Phys.* **2007**, *126*, 194311.
- [27] K. Pierloot, E. Van Besien, *J. Chem. Phys.* **2005**, *123*, 204309.
- [28] J. Tanti, M. Lincoln, A. Kerridge, *Inorganics* **2018**, *6*, 88.
- [29] V. V. Zhurov, E. A. Zhurova, A. A. Pinkerton, *Inorg. Chem.* **2011**, *50*, 6330–6333.
- [30] V. V. Zhurov, E. A. Zhurova, A. I. Stash, A. A. Pinkerton, *J. Phys. Chem. A* **2011**, *115*, 13016–13023.
- [31] D.-C. Sergentu, F. Gendron, E. D. Walter, S. Park, C. Capan, R. G. Surbella, C. Z. Soderquist, G. B. Hall, S. I. Sinkov, J. Autschbach, H. Cho, *Inorg. Chem.* **2022**, *61*, 3821–3831.
- [32] M. B. Andrews, C. L. Cahill, *CrystEngComm* **2013**, *15*, 3082–3086.
- [33] C. L. Cahill, N. P. Deifel, D. Reusser, L. Zhang, A. Navrotsky, *J. Chem. Thermodyn.* **2017**, *114*, 66–70.
- [34] D. D. Schnaars, R. E. Wilson, *Inorg. Chem.* **2013**, *52*, 14138–14147.
- [35] D. D. Schnaars, R. E. Wilson, *Inorg. Chem.* **2014**, *53*, 11036–11045.
- [36] M. M. Pynch, J. M. Williams, M. W. Kasperski, L. C. Applegate, T. Z. Forbes, *Inorganica Chim. Acta* **2020**, *508*, 119628.
- [37] L. J. Augustine, H. Rajapaksha, M. M. F. Pynch, M. Kasperski, T. Z. Forbes, S. E. Mason, *Inorg. Chem.* **2023**, *62*, 372–380.
- [38] H. Rajapaksha, L. J. Augustine, S. E. Mason, T. Z. Forbes, *Angew. Chem.* **2023**, e202305073.
- [39] E. Hashem, T. McCabe, C. Schulzke, R. J. Baker, *Dalton Trans* **2014**, *43*, 1125–1131.
- [40] J. A. Platts, R. J. Baker, *Phys. Chem. Chem. Phys.* **2018**, *20*, 15380–15388.
- [41] J. de Groot, K. Gojdas, D. K. Unruh, T. Z. Forbes, *Cryst. Growth Des.* **2014**, *14*, 1357–1365.
- [42] S. Biswas, S. Ma, S. Nuzzo, B. Twamley, A. T. Russell, J. A. Platts, F. Hartl, R. J. Baker, *Inorg. Chem.* **2017**, *56*, 14426–14437.
- [43] C. R. Groom, I. J. Bruno, M. P. Lightfoot, S. C. Ward, *Acta Crystallogr. Sect. B Struct. Sci. Cryst. Eng. Mater.* **2016**, *72*, 171–179.
- [44] E. V. Anslyn, D. A. Dougherty, *Modern Physical Organic Chemistry*, University Science Books, **2006**.
- [45] Ó. Rubio-Pons, L. Serrano-Andrés, M. Merchán, *J. Phys. Chem. A* **2001**, *105*, 9664–9673.
- [46] E. T. Ryan, T. Xiang, K. P. Johnston, M. A. Fox, *J. Phys. Chem. A* **1997**, *101*, 1827–1835.
- [47] J. Prochorow, B. Kozankiewicz, B. B. Dongo Gemi, O. Morawski, *Acta Phys. Pol. A* **1998**, *94*, 749–760.
- [48] K. Kasama, K. Kikuchi, S. Yamamoto, K. Ujiie, Y. Nishida, H. Kokubun, *J. Phys. Chem.* **1981**, *85*, 1291–1296.
- [49] K. Kikuchi, K. Kasama, A. Kanemoto, K. Ujiie, H. Kikubun, *J. Phys. Chem.* **1985**, *89*, 868–871.
- [50] K. Kikuchi, C. Sato, M. Watabe, H. Ikeda, Y. Takahashi, T. Miyashi, *J. Am. Chem. Soc.* **1993**, *115*, 5180–5184.
- [51] M. Andrews, D. Jones, A. Woodward, A. Swinburne, J. Lloyd, S. Magennis, S. Botchway, A. Ward, L. Natrajan, **2023**, DOI 10.26434/chemrxiv-2023-lvvtz.
- [52] J. O. Williams, B. P. Clarke, *J. Chem. Soc. Faraday Trans. 1 Phys. Chem. Condens. Phases* **1977**, *73*, 514.
- [53] J. R. Lakowicz, Ed. , in *Princ. Fluoresc. Spectrosc.*, Springer US, Boston, MA, **2006**, pp. 443–475.

- [54] V. Balzani, P. Ceroni, A. Juris, *Photochemistry and Photophysics: Concepts, Research, Applications*, John Wiley & Sons, **2014**.
- [55] M. Braun, W. Tuffentsammer, H. Wachtel, H. C. Wolf, *Chem. Phys. Lett.* **1999**, *303*, 157–164.
- [56] K. Ema, M. Inomata, Y. Kato, H. Kunugita, M. Era, *Phys. Rev. Lett.* **2008**, *100*, 257401.
- [57] CCDC deposition numbers: **2-Cl**, **3-Cl**, **5-Cl**, and **6-Cl** (CCDC 2309518, 2309519, 2309520, 2309521), and **2-Br**, **3-Br**, **5-Br**, and **6-Br** (CCDC 2309522, 2309523, 2309524, 2309525).

WILEY-VCH

Entry for the Table of Contents



Herein, we have employed a simple series of crystalline materials of the form $[\text{HAr}]_2[\text{UO}_2\text{X}_4]$ (Ar = aromatic N-heterocycle, X = Cl or Br) as a platform to study the influence of the outer-sphere cation HAr^+ on the photophysics of uranyl emission. Through a combination of experiment and density functional theory (DFT) calculations, we provide explanations for the distinct energy transfer pathways in each compound.

Institute and/or researcher Twitter usernames: @adharshraghavan, @Cahill_ArIva